nature communications

Article

https://doi.org/10.1038/s41467-025-67029-4

Cryogenic nanoscale visualization of intrinsic magnesium deposition in magnesium metal batteries

Received: 28 November 2024

Accepted: 14 November 2025

Published online: 16 December 2025

Check for updates

Gaoliang Yang[1,8], Tanmay Ghosh[1,8], Yuanjian Li[1], Zhengyu Ju[2], Carina Yi Jing Lim[3], Wen Ren[4], Zhi Chang[5], Jianbiao Wang[1], Jinliang Du[6], Ying Li[6], Chang Zhang[7], Wei Liu[7], Yan Yao[4] ✉, Guihua Yu[2] ✉ & Zhi Wei Seh[1] ✉

Magnesium metal batteries are considered promising candidates for next-generation energy storage systems due to the high volumetric capacity, intrinsic safety and natural abundance of magnesium. Yet, the fundamental mechanisms that govern the magnesium deposition and the formation of surface interphases remain poorly understood, largely due to the complexity of battery chemistry and the lack of reliable techniques to probe these processes at the atomic scale. Here we show that, by using cryogenic transmission electron microscopy, different magnesium deposition morphologies (e.g., whisker-shaped or seaweed-shaped) in conventional single-salt electrolytes converge to an intrinsic hexagonal platelet shape once surface passivation is decoupled from magnesium plating. This characteristic shape persists across different electrolyte chemistries, suggesting that suppressing surface passivation eliminates the influence of electrolyte composition on magnesium deposition morphology. These findings reveal the intrinsic nature of magnesium electrodeposition and establish a mechanistic link between interfacial chemistry and morphological evolution. Our work highlights a fundamental principle for controlling magnesium deposition behavior, paving the way for the rational design of stable, high-performance magnesium-based batteries.

Magnesium metal batteries (MMBs) offer a promising solution for efficient and sustainable energy storage systems, owing to their potential for higher volumetric energy density and utilization of cost-effective materials[1–3]. Unfortunately, the realization of high-performing MMBs is often hampered by their poor cycling performance arising from surface passivation of the magnesium (Mg) metal electrode. Mg metal readily reacts with electrolyte components due to its low electrochemical potential (−2.37 V vs. standard hydrogen electrode), forming a surface film on the Mg electrode[4,5]. Unlike lithium (Li) metal systems, where the solid-electrolyte interphase (SEI) is ionically conductive, the surface film formed on Mg electrode in conventional single-salt electrolytes is typically both electronically and ionically

[1]Institute of Materials Research and Engineering (IMRE), Agency for Science, Technology and Research (A*STAR), Singapore, Republic of Singapore. [2]Materials Science and Engineering Program and Walker Department of Mechanical Engineering, University of Texas at Austin, Austin, TX, USA. [3]Department of Materials Science and Engineering, Stanford University, Stanford, CA, USA. [4]Department of Electrical and Computer Engineering and Texas Center for Superconductivity at the University of Houston, University of Houston, Houston, TX, USA. [5]Department of Materials Physics and Chemistry, School of Materials Science & Engineering, Central South University, Changsha, Hunan, China. [6]Zhuhai Campus, Beijing Institute of Technology, Zhuhai, China. [7]School of Physical Science and Technology, ShanghaiTech University, Shanghai, China. [8]These authors contributed equally: Gaoliang Yang, Tanmay Ghosh. ✉e-mail: yyao4@uh.edu; ghyu@austin.utexas.edu; sehzw@a-star.edu.sg

insulating, resulting in electrode passivation and poor reversibility of Mg plating/stripping process[6,7]. Insights drawn from Li metal batteries have revealed that local chemistry and nanostructure of the interphase layer play a decisive role in governing metal growth dynamics[8,9]. Extending this paradigm to Mg systems highlights the critical need for a systematic investigation into both the physicochemical characteristics of the passivation layer and its direct influence on Mg nucleation and growth. Such studies are essential to elucidate the fundamental mechanisms underlying Mg deposition and to develop targeted strategies that mitigate passivation-induced limitations for MMBs.

Extensive efforts have been devoted in recent years to probing the interfacial chemistry and deposition dynamics of Mg anodes using a variety of techniques. Electrochemical analyses have revealed the impact of overpotentials and Coulombic efficiency on assessing reversibility and interfacial phenomena[10,11], while spectroscopic studies [e.g., X-ray photoelectron spectroscopy (XPS), time-of-flight secondary ion mass spectrometry (ToF-SIMS)] have identified surface species that impede ion transport and contribute to electrode passivation[12–14]. In situ and operando techniques, including optical microscopy[15], atomic force microscopy (AFM)[16], and electrochemical quartz crystal microbalance (EQCM)[17], have shed light on dynamic changes in surface morphology and mass transfer. Complementary computational studies have elucidated the roles of solvation structures, de-solvation energies, and interfacial kinetics[18,19]. Despite these advances, a direct correlation between electrolyte chemistry, interfacial passivation, and the resulting deposition morphology remains poorly understood. In this context, cryogenic transmission electron microscopy (cryo-TEM) provides a unique opportunity to observe the Mg deposits and the interfacial structures at near-native states preserved under cryogenic conditions with high spatial resolutions[20–22]. The adoption of cryo-TEM seeks to complement existing experimental and computational knowledge by directly visualizing the morphological and interfacial consequences of electrolyte modulation, thereby enabling to establish a robust "composition-structure-performance" framework that is essential for guiding the rational design of next-generation electrolyte systems for durable MMBs.

Herein, we perform detailed morphological and structural characterizations on Mg deposits and the concomitant surface interphase layers in various electrolyte systems using cryo-TEM. Different Mg deposition morphologies are observed to converge to an intrinsic hexagonal platelet shape when surface passivation is decoupled from Mg plating. We begin our study using a representative magnesium triflate ($Mg(OTf)_2$)/1,2-dimethoxyethane (DME) electrolyte, where whisker-shaped Mg deposits are unexpectedly observed. This unusual morphology may arise from the formation of a compact MgO-based passivation layer on the surface of the Mg deposits. Surprisingly, a plate-stacked morphology is favored over these whisker-shaped Mg deposits when surface passivation is highly suppressed by Cl^- or BH_4^- additive modulation. Cryo-TEM quantitatively characterizes this morphology to be well-defined hexagonal platelets, aligning with the theoretical Wulff structure prediction of a hexagonal close-packed (HCP) metal. Encouragingly, we found that Mg deposits with suppressed surface passivation exhibit consistent hexagonal platelet morphology across different electrolyte chemistries, indicating an intrinsic deposition tendency of HCP Mg metal. These findings may explain the prevailing recognition of Mg metal as a "dendrite-free" anode in most electrolyte systems applicable to MMBs.

Results

Morphological evolution of whisker-shaped Mg deposits

Whilst Li metal systems are plagued by dendritic Li growth during electrodeposition, Mg holds promise as an alternative anode due to its reputedly "non-dendritic" nature. This is attributed to the lower diffusion barrier for Mg atoms, yielding a smooth surface with mobile transfer of Mg atoms during deposition[23,24]. Dendritic Mg deposition has traditionally been considered rare, typically observed only in specific electrolytes such as Grignard-based systems and/or under extreme operating conditions (e.g., high current densities or elevated self-diffusion rates)[15,25]. However, recent studies have revealed that dendritic features can also emerge under more moderate and practically relevant conditions in conventional single-salt electrolytes [e.g., magnesium bis(trifluoromethanesulfonimide) ($Mg(TFSI)_2$)][12,26]. Beyond highlighting the significance of Mg deposition during electrochemical cycling, detailed investigation into the passivated surface structure has also been conducted through the cryo-TEM characterization[12,27]. Despite these advancements, the role of local interface chemistry in governing Mg deposition behavior remains elusive, especially in single-salt electrolyte systems.

Given that $Mg(OTf)_2$ possesses stronger anti-reduction and hydrophobicity properties compared to $Mg(TFSI)_2$[28–31], a single-salt $Mg(OTf)_2$/DME electrolyte was chosen as a model system to investigate the Mg deposition morphology using scanning electron microscopy (SEM). As shown in Supplementary Fig. 1, whisker-shaped Mg deposits are unexpectedly observed in the $Mg(OTf)_2$ electrolyte at 0.5 mA cm^{-2}, a morphology that has rarely been reported in MMBs. The whisker-shaped Mg deposits observed challenge previous hypotheses regarding the differences in deposition behaviors between Mg and other alkali metals (e.g., Li)[23,24,32], demonstrating that similar whisker-shaped deposition can still occur in both systems despite significantly different metallic properties. Similar to Li metal batteries, the formation of whisker-shaped Mg deposits substantially increases the specific surface area, thereby accelerating parasitic reactions with the electrolyte, which depletes the Mg sources and exacerbates the poor reversibility of Mg anodes[33]. Moreover, this whisker-like growth also poses safety risk due to the potential to induce cell shorting[33]. The morphological evolution of the whisker-shaped Mg deposits in $Mg(OTf)_2$ electrolyte at different deposition stages was further investigated by SEM. As displayed in Supplementary Fig. 2, the whisker-like morphology of Mg deposits is maintained throughout continuous deposition from 5 min to 20 min. Interestingly, the Mg deposit size remains nearly unchanged from 5 min (0.042 mAh cm^{-2}) to 15 min (0.125 mAh cm^{-2}), but grows significantly at 20 min (0.167 mAh cm^{-2}).

Cryo-TEM was leveraged to further investigate Mg deposition behavior at the single-particle level. At the initial Mg nucleation stage (~1 min), single Mg nuclei (~50 nm diameter) or clusters of nuclei are observed (Supplementary Fig. 3). The Mg nuclei subsequently assemble into porous Mg whiskers (5 min; Fig. 1a_1–a_3) and gradually aggregate into denser whiskers (10 min; Fig. 1b_1–b_3). Consistent with the SEM results in Supplementary Fig. 2, at 15 min, further densification of the Mg whiskers is observed with minimal dimensional changes (Fig. 1c_1–c_3), while lateral growth occurs with continuous deposition beyond 15 min (0.125 mAh cm^{-2}) (Fig. 1d_1–d_3). The observed growth behavior, transitioning from porous to dense states, significantly differs from analogous whisker-like Li deposition, which may be attributed to the different electrode-electrolyte interphase structures[8,34]. In addition to imaging characterization, cryo-scanning TEM (cryo-STEM) coupled with energy dispersive X-ray spectroscopy (EDS) mapping was conducted. The mapping images reflect a homogeneous distribution of measured elements (Supplementary Figs. 4–7), among which Mg is expectedly the primary element. Interestingly, oxygen (O) is identified as the second most predominant element, suggesting that the surface interphases may mainly consist of O-based compounds.

Microstructure of the passivated interphase

To characterize the detailed structure of passivation layers on Mg deposits at the single-grain level, high-resolution TEM (HRTEM) was utilized to reveal their native state under cryogenic conditions. The cryo-TEM image in Fig. 2a shows that the whisker-shaped Mg deposit is composed of numerous nanograins containing metallic Mg and MgO,

https://doi.org/10.1038/s41467-025-67029-4

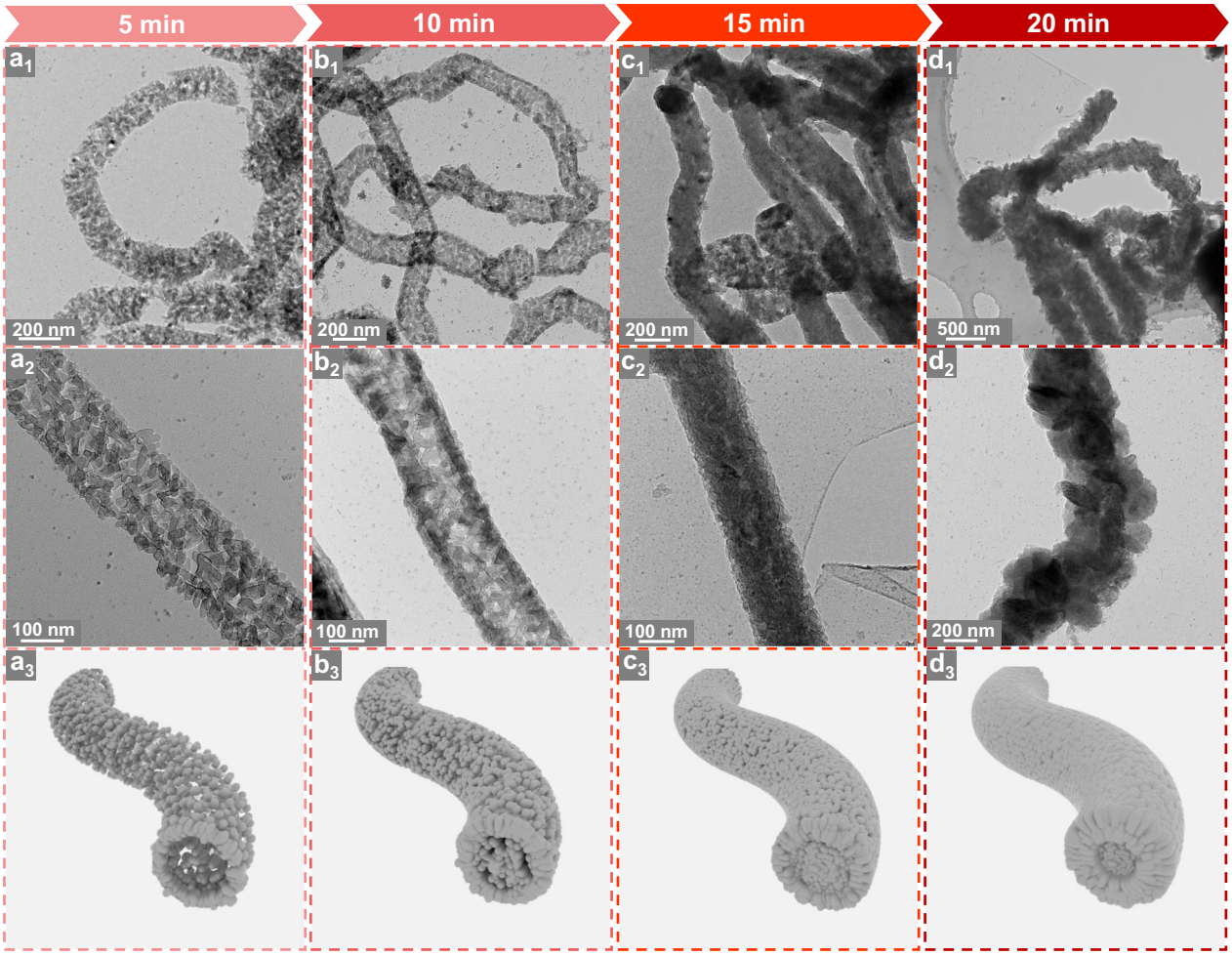

Fig. 1 | The morphological evolution of whisker-shaped Mg deposits in pure $Mg(OTf)_2$ electrolyte. Cryo-TEM characterization of whisker-shaped Mg deposits under different deposition stages at 0.5 mA cm^{-2}. **a_1**, **a_2** 5 min deposition; **b_1**, **b_2** 10 min deposition; **c_1**, **c_2** 15 min deposition and (**d_1**, **d_2**) 20 min deposition. **a_3**–**d_3** Schematic of the whisker-shaped Mg deposits under the corresponding deposition stages.

as further confirmed by the selected area electron diffraction (SAED) pattern (inset in Fig. 2a). A compact, continuous layer is observed on the nanograin surface from the enlarged image (Fig. 2b). The cryo-HRTEM image in Fig. 2c demonstrates that each nanograin within the Mg whisker consists of two distinct regions. The inner region mainly consists of highly crystalline Mg phases, as verified by fast Fourier transform (FFT) and lattice spacing measurements (Fig. 2d). A smooth, thin layer (~3 nm thickness), appearing slightly darker, is identified as the passivation layer formed on Mg deposit surface during deposition. This layer exhibits a continuous structure with nanoscale regimes of crystalline species (Fig. 2c). According to the measurements of lattice spacings and FFT data (Fig. 2e), these crystalline species on the surface regions are identified to be MgO, consistent with the SAED results (inset in Fig. 2a). The distribution of Mg metal and MgO layer is more apparent in the inverse FFT images (Fig. 2g), further confirming the presence of a compact MgO passivation layer on the outer surface of Mg nanograins. To directly probe the bonding environment of above structures, cryo-STEM electron energy loss spectroscopy (EELS) was conducted on the whisker-shaped Mg deposits (Supplementary Figs. 8, 9). The analyses highlight a clear compositional contrast between the metallic Mg core and the MgO shell of the nanograins (Fig. 2f). The dominance of MgO in the passivation layer can be attributed to side reactions involving anion/solvent and trace H_2O impurities on the surface of Mg deposits (*vide infra*)[12,35]. However, no lattice signals corresponding to MgF_2 or MgS are detected in the passivation layer, which may be attributed to the low content (Supplementary Fig. 6) or poor crystallinity.

Hexagonal platelet deposits by decoupling surface passivation

As the Mg^{2+}-insulating passivation film is detrimental to cycling performance, one of the most significant topics for MMBs is suppressing the passivation between electrolytes and Mg metal anodes. Electrolyte modification with effective additives is a predominant strategy in MMBs to mitigate surface passivation and regulate deposition behavior[2,5]. However, the current understanding of the role of additives is limited to relatively macroscopic characterizations or theoretical hypotheses[6,36], while their exact effects on interfacial processes are still not fully understood. Therefore, employing magnesium chloride ($MgCl_2$) as a representative additive to suppress passivation[37–39], we performed detailed characterization of the Mg deposits obtained from the $MgCl_2$-containing electrolyte. In stark contrast to the whisker-shaped Mg deposits in $Mg(OTf)_2$ electrolyte, the Mg deposits in $Mg(OTf)_2 + MgCl_2$ electrolyte are found to be plate-stacked particles from the SEM images in Fig. 3a and Supplementary Fig. 10. Cryo-TEM images (Fig. 3b–d) further reveal that these Mg particles are composed of hexagonal platelets, while the corresponding SAED pattern (Fig. 3e) indicates their preferential alignment along the <002> zone axis. This hexagonal platelet structure stems from a lower thermodynamic free energy associated with the exposed closest-packed (002) plane of the HCP Mg metal[33,40,41]. This phenomenon is further validated by the well-

https://doi.org/10.1038/s41467-025-67029-4

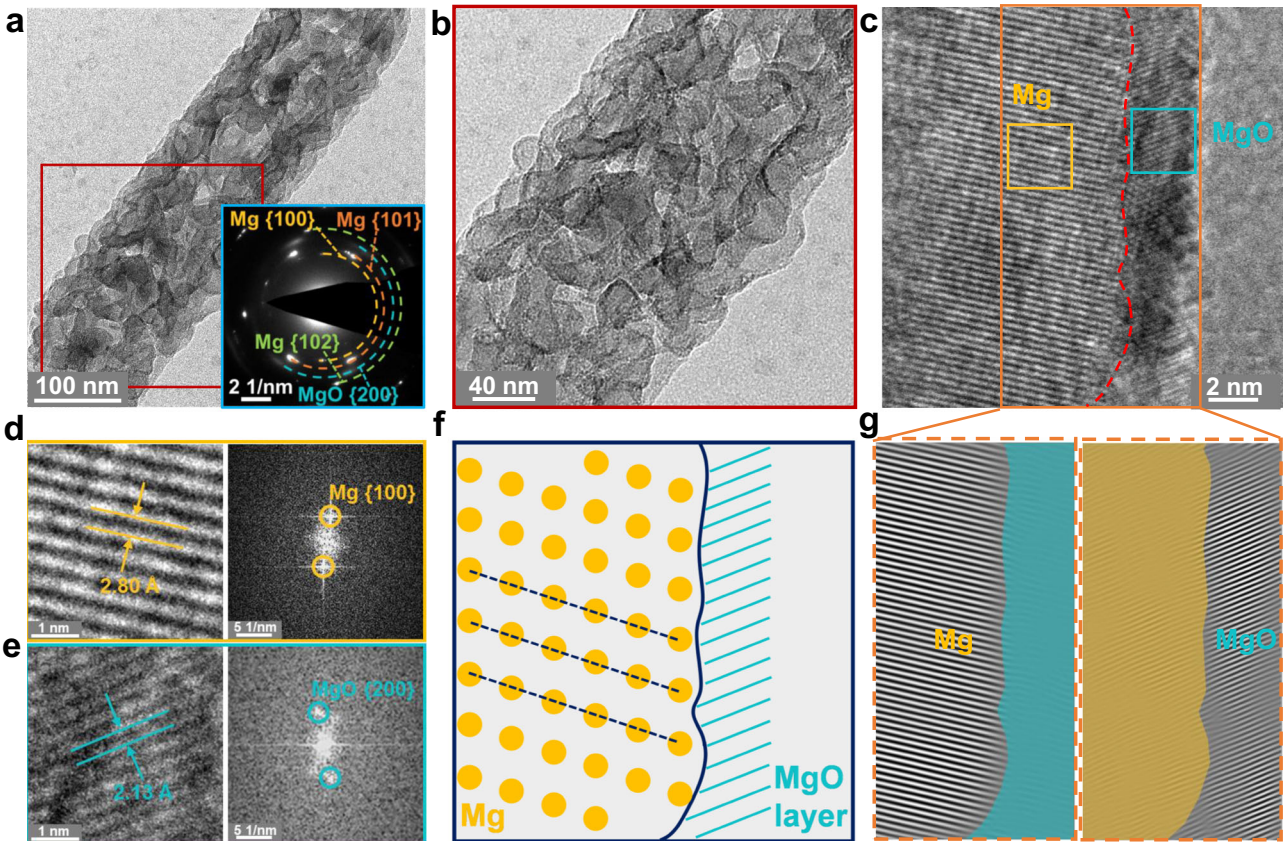

Fig. 2 | Microstructure of the whisker-shaped Mg deposits and passivated interphases in pure $Mg(OTf)_2$ electrolyte. a, **b** Cryo-TEM images (the inset in Fig. 2a is the corresponding SAED pattern) and (**c**) cryo-HRTEM image of the whisker-shaped Mg deposit. **d**, **e** Magnified images of boxed regions in yellow (metallic Mg) and blue (MgO layer) from Fig. 2c and corresponding FFT images. **f** Schematic of the nanograin structure from the whisker-shaped Mg deposit. **g** The inverse FFT images of selected region in brown from Fig. 2c. The shaded areas in yellow and blue colors are the corresponding metallic Mg and MgO layer of the brown region in (**c**).

defined hexagonal platelet shape under less stacked conditions (Supplementary Fig. 11a), which is oriented normal to the [002] direction as observed from the electron diffraction pattern (Supplementary Fig. 11b). This observation aligns well with the thermodynamic Wulff construction of an HCP metal[42].

According to the insights drawn from other metal batteries (e.g., Li), deposition morphology is immensely influenced by the local chemistry and structure of the interphase between anode and electrolyte[8,9]. The further enlarged cryo-TEM image indicates a relatively rough surface with sparse coverage of the plate (Fig. 3d), which is distinctly different from the whisker-shaped Mg deposits. Instead of a continuous and compact MgO-based passivation layer, the surface interphase layer is embedded with several randomly arranged crystalline domains (~2 nm) (Fig. 3f), which are identified as MgO nanograins from the lattice fringes and corresponding FFT images (Fig. 3h, j). A distinct signal assigned to metallic Mg is found in the interphase layer based on the FFT images from region III and V (Fig. 3i, k). Combined with the randomly distributed MgO domains, it is reasonable to propose that this surface interphase layer results from the inevitable chemical reaction between the freshly deposited Mg and liquid electrolyte (Fig. 3l)[12,22]. This hypothesis is further supported by cryo-TEM analyses across different electrolyte systems (Supplementary Figs. 15–22, *vide infra*), which verify that the Mg deposition morphology and surface interphase remain consistent. Moreover, the cryo-HRTEM image of the inner layer (Fig. 3g) is indexed to single-crystalline Mg with a lattice spacing of 2.77 Å, corresponding to the Mg {100} side plane, further validating the hexagonal platelets deposition morphology.

In addition, the chemical compositions of the surface interphases in different electrolytes were characterized by EDS measurement. The EDS maps (Supplementary Fig. 12) display a homogeneous elemental distribution across the deposit surface obtained from $Mg(OTf)_2 + MgCl_2$ electrolyte. The ratios of C, O, F and S elements are considerably lower than those in $Mg(OTf)_2$ electrolyte (Supplementary Fig. 6), further suggesting that the surface interphase on Mg deposits formed with $MgCl_2$ addition likely arises from the chemical reaction between freshly deposited Mg and electrolyte, rather than electrolyte-derived electrochemical decomposition[12,22]. Notably, Cl signals are detected on the surface of Mg deposits from the $MgCl_2$-containing electrolyte (Supplementary Fig. 12), which can be attributed to the surface-adsorbed chloride species from the electrolyte. This result supports the prior claim that Cl-containing species reduce the accessibility of reactive electrolyte components to the anode surface, thereby protecting it from electrolyte decomposition[6,43]. Based on the cryo-TEM observations and recent theoretical studies, the dominant effects of $MgCl_2$ on modulating Mg deposition behavior can be summarized as follows: (1) The addition of $MgCl_2$ alters the solvation structure of Mg^{2+} ions, forming Mg–Cl complex species (e.g., $[MgCl]^+$, $[Mg_2Cl_3]^+$)[36]. These complexes reduce the de-solvation energy barrier and suppress solvent/anion decomposition at the electrode interface, facilitating more uniform Mg^{2+} reduction and nucleation. (2) Cl-based species may weakly adsorb onto the Mg surface during deposition, locally modifying the interfacial energy and suppressing the growth of Mg protrusions.

https://doi.org/10.1038/s41467-025-67029-4

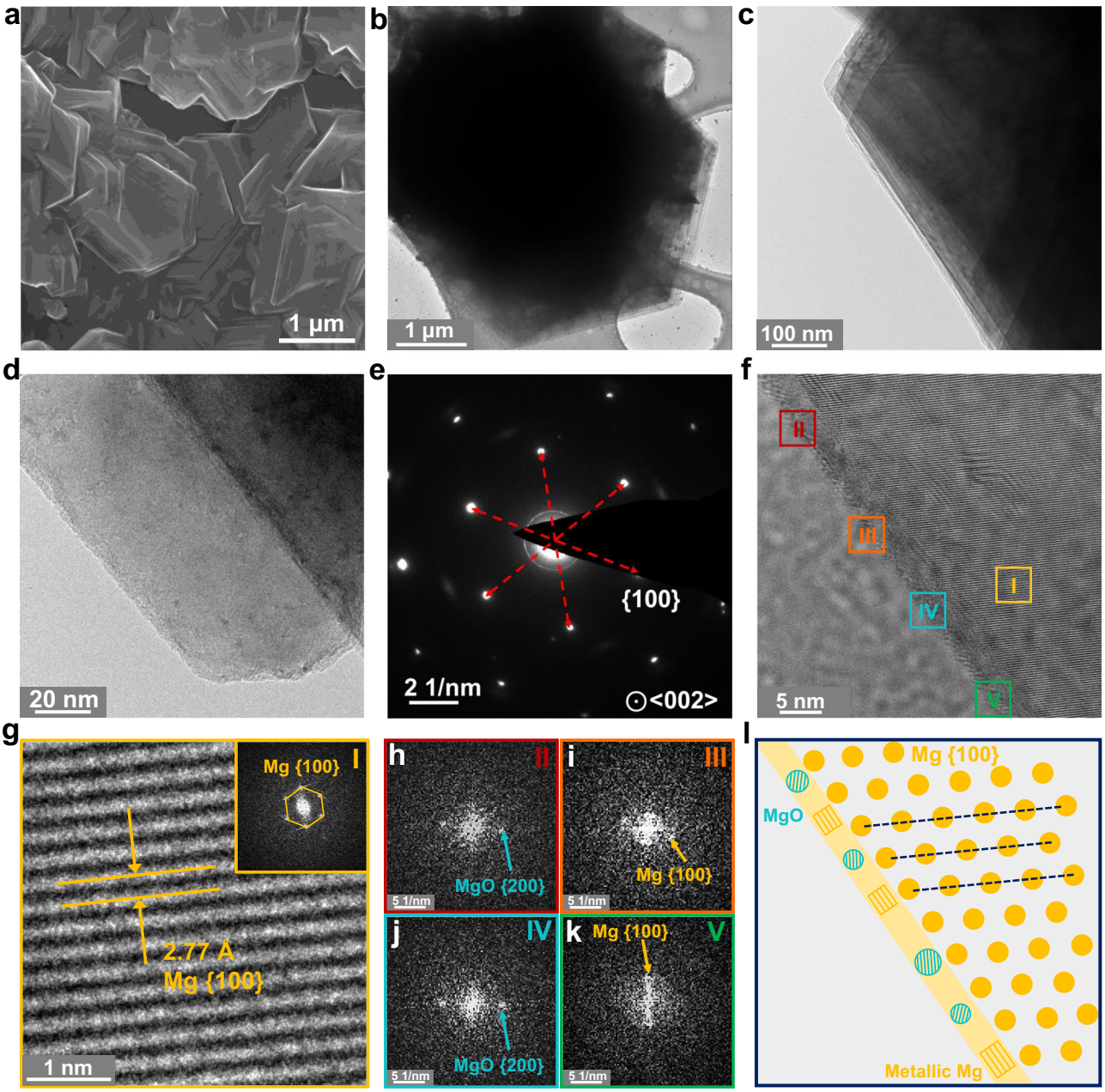

Fig. 3 | Microstructure of the Mg deposits and the corresponding surface interphase in $Mg(OTf)_2 + MgCl_2$ electrolyte. a SEM image of the plate-shaped Mg deposits. **b**–**d** Cryo-TEM images with different magnifications. **e** The corresponding SAED pattern showing the alignment along the <002> zone axis. **f** Cryo-HRTEM image of the observed structure on Mg hexagonal platelets in $Mg(OTf)_2 + MgCl_2$ electrolyte. **g** Magnified cryo-HRTEM image of yellow region I (Mg metal) outlined in (**f**) and inset is the corresponding FFT image. **h**–**k** Corresponding FFT images from different regions in (**f**). **l** Schematic of the interphase structure on deposited Mg hexagonal platelets.

Intrinsic Mg deposition across various electrolyte systems

Given that Mg deposition morphology shifts from whisker-like to hexagonal platelet upon the suppression of surface passivation in $Mg(OTf)_2$-based electrolytes, we further explored whether this phenomenon is universal by examining two additional single-salt [i.e., $Mg(TFSI)_2$ and magnesium bis(hexamethyldisilazide) ($Mg(HMDS)_2$)] electrolyte systems. As shown in Supplementary Fig. 13, seaweed-like Mg deposits are observed in the $Mg(TFSI)_2$ electrolyte, consistent with previous reports[12]. A thick passivation layer composed of MgF_2 and MgO is evident on the surface of the Mg deposits (Supplementary Fig. 13d–h), which hinders ion transport and results in large overpotentials and low Mg utilization[12]. With the addition of 0.1 M $MgCl_2$, although electrolyte decomposition is somewhat suppressed, a passivation layer (~10 nm) persists on the Mg deposit surface (Supplementary Fig. 14). Intriguingly, a morphological transition from seaweed-like to plate-shaped is also observed in $Mg(TFSI)_2 + 0.1$ M $MgCl_2$ electrolyte (Supplementary Fig. 14b, c), further confirming the critical role of the surface interphase in governing Mg deposition. When the $MgCl_2$ concentration is increased to 0.4 M to further suppress surface passivation, a similar hexagonal plate morphology is observed (Supplementary Fig. 15), consistent with the deposition behavior in $Mg(OTf)_2$-based electrolytes. For $Mg(HMDS)_2$-based electrolytes, although Mg cannot normally be deposited at 0.5 mA cm^{-2} in pure $Mg(HMDS)_2$ electrolyte due to severe passivation (Supplementary Fig. 16)[44], similar hexagonal plate morphology and surface interphase are obtained with the $MgCl_2$ addition (Supplementary Fig. 17).

https://doi.org/10.1038/s41467-025-67029-4

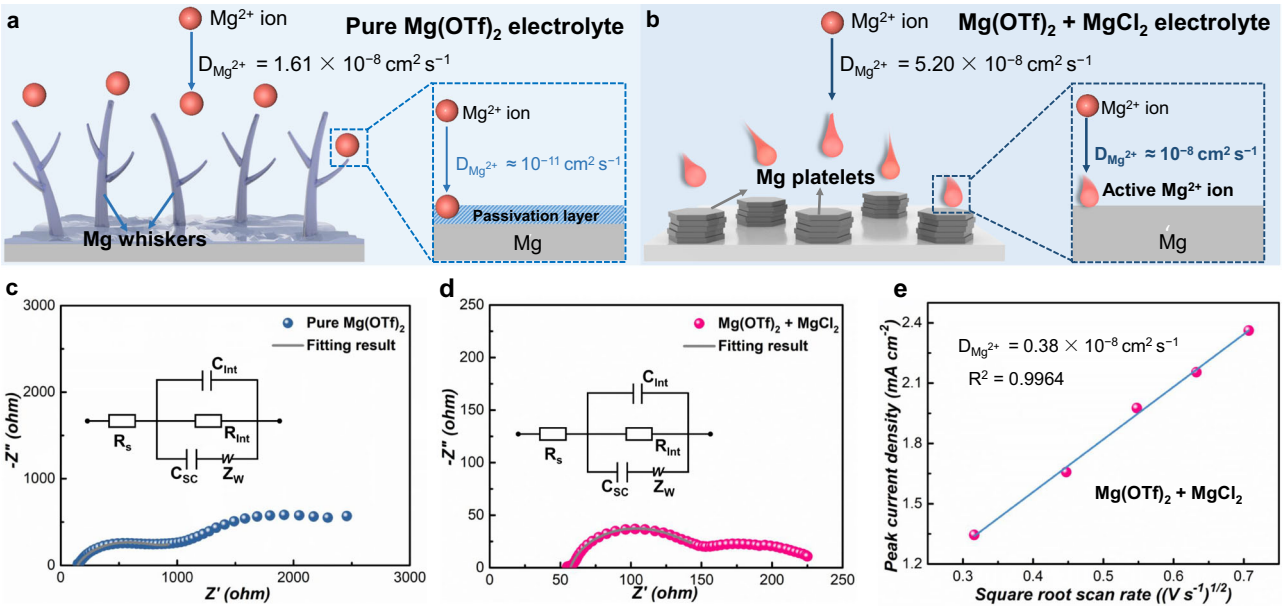

Fig. 4 | Electrochemical analysis of Mg deposition pathways in different electrolytes. a Schematic of Mg^{2+} transport from electrolyte to electrode surface with serious surface passivation in pure $Mg(OTf)_2$ electrolyte and (**b**) with suppressed passivation in $Mg(OTf)_2 + MgCl_2$ electrolyte. Nyquist plot of the EIS and the fitting results for the Mg cells with (**c**) pure $Mg(OTf)_2$ electrolyte and (**d**) $Mg(OTf)_2 + MgCl_2$ electrolyte; the inset is the equivalent circuit model for the surface interphase and the fitting results are summarized in Supplementary Table 3. **e** Linear regression of the peak current with the square root of the scan rate derived from LSV profiles for Mg electrodeposition. Source data for (**c**–**e**) are provided as a Source Data file.

Furthermore, to exclude the possibility that the hexagonal plate morphology is specific to chloride-based electrolytes, a chloride-free additive, tetrabutylammonium borohydride ($TBABH_4$), was employed as an alternative additive[44]. As displayed in Supplementary Figs. 18–20, Mg metal is also deposited as hexagonal plates with similar interphase properties compare to those in single-salt Mg electrolytes modified with $MgCl_2$ additives. Encouragingly, this phenomenon can be extended to other electrolyte systems beyond the conventional single-salt electrolytes, such as all phenyl complex (APC) and magnesium tetrakis(hexafluoroisopropyloxy)borate ($Mg[B(hfip)_4]_2$) electrolytes (Supplementary Figs. 21, 22), two representative non-passivating electrolytes that are widely applied in MMBs[45,46]. Thus, we can conclude that electrolyte chemistry poses negligible influence on the deposition morphology with minimal surface passivation. Indeed, these hexagonal Mg plates exhibit similar features across various electrolyte systems (e.g., differing in salts, solvents, and solvation structures), suggesting three important findings: (i) The deposition morphology is mostly independent of electrolyte chemistries when surface passivation is suppressed. (ii) The hexagonal plates represent the intrinsic deposition morphology of Mg metal in the absence of passivation influence. (iii) The interphase properties strongly govern Mg deposition morphology. Additional experiments conducted on different current collectors confirm that the deposition morphology remains consistent regardless of the substrate material (Supplementary Fig. 23). The interfacial characteristics between the substrate and the Mg deposits closely resembles the surface interphases on Mg deposits, highlighting that interfacial passivation is effectively suppressed in the presence of $MgCl_2$ additives (Supplementary Figs.24–26, Supplementary Note 4). This observation indicates that while substrate effects are non-negligible, the electrolyte-mediated interfacial environment plays a more decisive role in dictating Mg deposition behavior, which is consistent with our overall findings in this work.

Electrochemical analysis of different Mg deposition pathways

To further investigate the influence of surface interphases on Mg electrodeposition, Mg^{2+} transport from the bulk to the depositing metallic Mg surface was evaluated in different electrolytes. From the fitted electrochemical impedance spectroscopy (EIS) spectra after deposition (Fig. 4c, d, Supplementary Table 3), the ionic resistance of the interphase layer in $Mg(OTf)_2 + MgCl_2$ electrolyte (82 Ω) is much smaller than that in $Mg(OTf)_2$ electrolyte (710 Ω). Compared with the compact passivation layer in $Mg(OTf)_2$ electrolyte, the depassivated interphase (Fig. 3f) may provide abundant transport channels for Mg^{2+} ions, thereby facilitating their migration to the metal surface. Since cation diffusion coefficients (D_{Mg2+}) in the solid (interphase layer) and liquid (electrolyte) phase vary by orders of magnitude (Fig. 4a, b), the D_{Mg2+} values of the liquid electrolytes were first quantified using the chronocoulometry (CC) method (see Methods for details)[19,26]. From the slope of the resulting Anson plot (Supplementary Fig. 27a), the D_{Mg2+} is determined to be 1.61×10^{-8} cm^2 s^{-1} for pure $Mg(OTf)_2$ electrolyte. With the addition of $MgCl_2$, a much higher D_{Mg2+} of 5.20×10^{-8} cm^2 s^{-1} is obtained (Supplementary Fig. 27b), due to the profound effects of Cl ions on the coordinated solvation structure, where a typical $[Mg_2Cl_3]^+$ dimer is formed[37].

To evaluate Mg^{2+} transport to the Mg metal surface in different electrolytes, interfacial impedance spectra of respective Mg deposits (Fig. 4c, d) were further analyzed to calculate the D_{Mg2+} through the surface interphase layers (see Methods for details)[22,47,48]. D_{Mg2+} from the bulk to the Mg surface in $Mg(OTf)_2$ electrolyte was calculated to be 4.78×10^{-11} cm^2 s^{-1} (Fig. 4a). Since cation transport across the surface interphase layer accounts for the majority of the interfacial impedance[49], the dramatic decrease in D_{Mg2+} shows that the passivation layer severely impedes Mg^{2+} transport in pure $Mg(OTf)_2$ electrolyte. In contrast, the D_{Mg2+} from the bulk to the Mg deposits surface in $Mg(OTf)_2 + MgCl_2$ electrolyte is calculated to be 0.29×10^{-8} cm^2 s^{-1} (Fig. 4b), which is substantially higher than that in pure $Mg(OTf)_2$ electrolyte and on the same order of magnitude as the D_{Mg2+} in liquid electrolytes. The enhanced D_{Mg2+} reflects significantly facilitated Mg^{2+} transport to the Mg-electrolyte interface due to the suppressed surface passivation in the presence of $MgCl_2$. To further validate these findings for the $Mg(OTf)_2 + MgCl_2$ electrolyte, linear sweep voltammetry (LSV) measurements were

https://doi.org/10.1038/s41467-025-67029-4

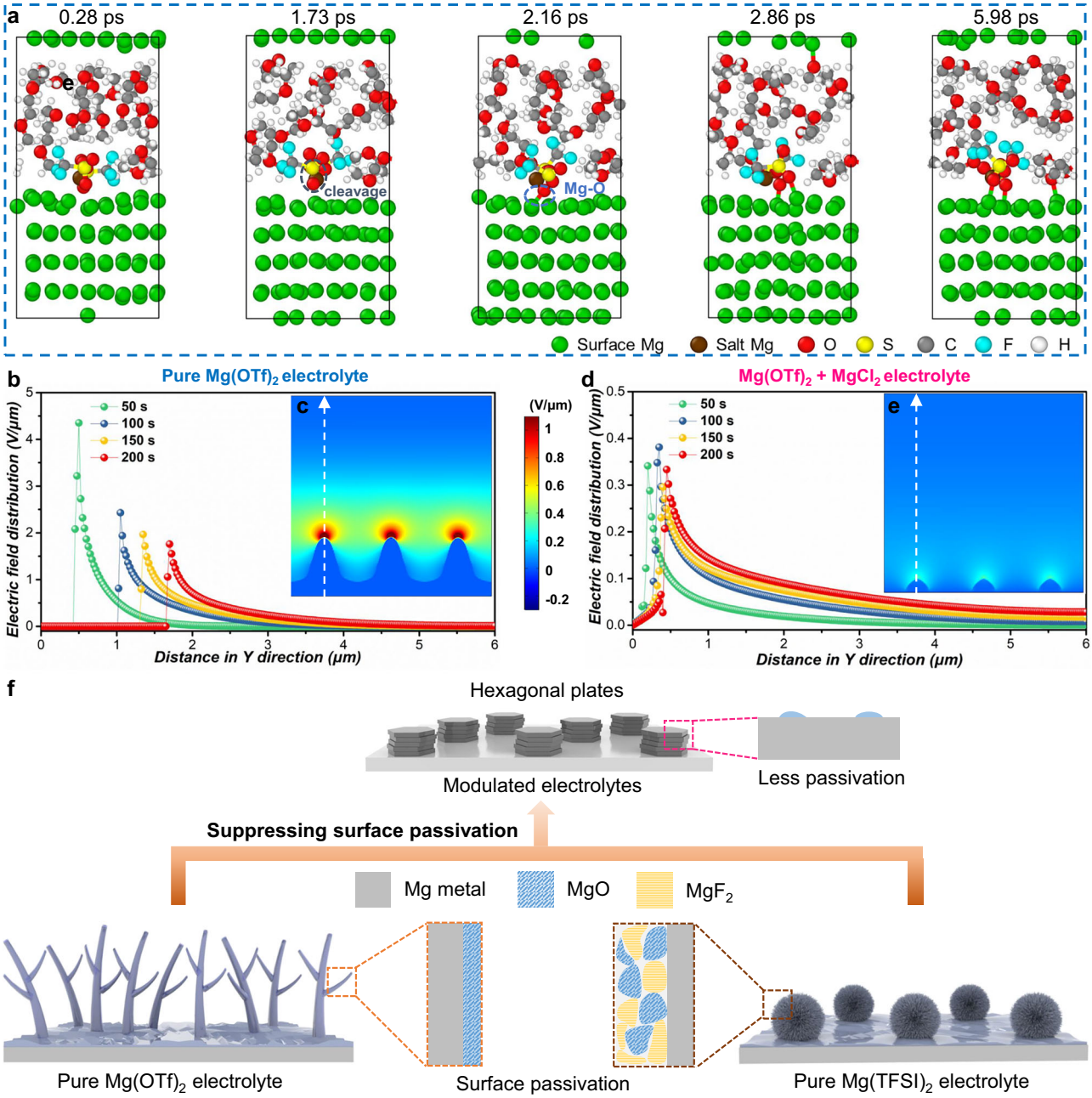

Fig. 5 | Simulation and schematic illustration of deposition behaviors in different electrolytes. a Representative snapshots at various timescales from AIMD simulation showing the reductive reaction pathway of $Mg(OTf)_2$/DME electrolyte with Mg metal. The initial structure of the AIMD simulation is provided as Supplementary Data 1. The electric field distributions along with tip direction (white dashed lines) at different deposition timesteps and the 2D electric field profiles for Mg deposition at 200 s in $Mg(OTf)_2$ electrolytes of (**b**, **c**) without and (**d**, **e**) with $MgCl_2$. **f** Schematic of transition of different Mg deposition morphologies to similar stacked Mg hexagonal plates independent of electrolyte chemistry. Source data for (**b**) and (**d**) are provided as a Source Data file.

performed at scan rates ranging from 0.1 to 0.5 V s^{-1}. The peak current densities in Supplementary Fig. 28 display a linear relation with the square root of scan rates (Fig. 4e), from which a D_{Mg2+} value of 0.38×10^{-8} cm^2 s^{-1} is calculated (see Methods for details)[48]. The consistent D_{Mg2+} values derived from EIS and LSV corroborate that the Mg^{2+} transfer kinetics across the surface interphases can be enhanced to the same order of magnitude as bulk liquid diffusion when surface passivation is suppressed. Owing to the optimized deposition and enhanced interfacial diffusion, the cycling performance is significantly improved by additive modification, as evidenced by the enhanced cycling stability and markedly reduced overpotential compared with the blank electrolytes (Supplementary Figs. 29–31).

Simulation and schematic illustration of deposition behavior

To investigate the origin of the MgO-based passivation layers, ab initio molecular dynamics (AIMD) simulations were employed to elucidate the interfacial reaction mechanism between the $Mg(OTf)_2$/DME electrolyte and the Mg metal. The snapshots in Fig. 5a show the temporal evolution of the system at different simulation timescales. Both the OTf^- anion and DME solvent were observed to spontaneously adsorb onto the surface of Mg metal. The initial step of the decomposition pathway involves the cleavage of the S-O bond in the OTf^- moiety at ~1.73 ps, resulting in the formation of SO_2CF_3 fragments and individual O atoms[50]. The isolated O atoms can easily adsorb onto the Mg anode surface, initiating the formation of MgO species. With the increasing of the simulation time, the O atoms derived from both OTf^- anion and

DME solvent continue to interact with Mg metal, leading to the progressive formation of MgO species. Therefore, the simulation results indicate that OTf^- anion and DME solvent can both undergo in situ chemical reactions with Mg metal, resulting in the formation of an MgO-rich passivation layer, consistent with the experimental observations. In addition, the presence of trace water in the electrolyte (Supplementary Table 1) may also accelerate this process, further promoting the formation of MgO-dominated passivation layer on Mg deposits in $Mg(OTf)_2$/DME electrolyte[35].

To validate the effects of passivated interphase on the early stages of Mg deposition, molecular dynamics (MD) simulations were conducted to analyze Mg nucleation and growth at the nanoscale in different electrolytes (Supplementary Figs. 32, 33). Generally, Mg nucleation occurs on the current collector, where Mg^{2+} ions migrate and are subsequent reduced to Mg atoms. Due to the inevitable side reactions between the newly formed Mg nuclei and electrolyte components, a compact MgO-rich passivation layer forms on the nucleus surface in pure $Mg(OTf)_2$ electrolyte. Given the sluggish ion transport kinetics of this passivation layer, the flux of Mg^{2+} ions to the nucleus surface gradually stalls[51]. Consequently, Mg^{2+} ions tend to localize and are preferentially reduced at the Mg particle-electrolyte interface,[52] leading to the sprouting of particle-on-particle growth and finally forming the whisker-shaped Mg deposits (Supplementary Fig. 32, the initial structure of the MD simulation is provided as Supplementary Data 2)[53]. In the presence of $MgCl_2$ additives, surface passivation reactions can be effectively suppressed, thereby facilitating Mg^{2+} transfer at the electrolyte-electrode interface. As such, the deposited Mg nuclei can continuously grow and merge at the electrode-electrolyte interface, allowing the intrinsic growth mode of an HCP metal to form the plate-shaped Mg deposits (Supplementary Fig. 33, the initial structure of the MD simulation is provided as Supplementary Data 3)[54]. The MD simulation demonstrates significant differences in the initial Mg nucleation and growth processes across different electrolyte systems, further emphasizing the crucial role of surface interphase in governing deposition behavior.

The Mg deposition processes in different electrolytes were further simulated and reproduced by phase-field simulations based on practical electrochemical conditions. The models developed herein did not involve the surface interphase as a third phase. Instead, the effects of the surface interphase in the models were integrated by adjusting the ionic diffusion coefficient near the reaction interface[51]. Consistent with the experimental results, whisker-shaped Mg deposits gradually form over time in pure $Mg(OTf)_2$ electrolyte (Supplementary Fig. 34a–d), whereas a faceted morphology (Supplementary Fig. 34e–h) is observed for Mg deposits in $Mg(OTf)_2 + MgCl_2$ electrolyte. This morphological difference is directly associated with the temporal evolution of the electrochemical driving forces at the growth surface (Fig. 5b–e), which can be further analyzed from their local ion concentration and electric field distributions[55]. As illustrated in Supplementary Fig. 35, severe cation concentration polarizations are observed near the growing tip regions in pure $Mg(OTf)_2$ electrolyte, whereas the cation concentration gradient is significantly homogenized at the electrode surface for the electrolyte with $MgCl_2$ (Supplementary Fig. 36). The high cation concentration gradient near the growth region may also result in the uneven electric field distribution, which can be further visualized from the electric field profiles. As shown in Supplementary Fig. 35b and 36b, the potential drops at anode surface region due to charge-transfer reaction, creating an elevated electric field at anode/electrolyte interfacial region (Fig. 5c and 5e). The electric field variation along tip directions in pure $Mg(OTf)_2$ electrolyte show that the electric field strength in the tip region is strongest at the initial stage of deposition (Fig. 5b), triggering the subsequent deposition with sharp tip morphology. In contrast, the electric field strength in the tip region maintains constant during the deposition for $Mg(OTf)_2 + MgCl_2$ electrolyte (Fig. 5d). Additionally, the intensity of electric field is also much lower than that in the pure $Mg(OTf)_2$ electrolyte during the whole process, thereby facilitating the homogeneous deposition with faceted morphology. The simulation results verify that the pronounced differences in deposition morphology across various electrolytes are attributed to the different ion concentration gradients and electric field strength, which may originate from the distinct anode-electrolyte interphases. The combination of various simulation approaches exhibits excellent consistency with experimental observations at each stage of the deposition process, offering a comprehensive and mechanistic understanding of Mg deposition across multiple scales. This integrated computational–experimental framework provides critical insights into interfacial phenomena and their influence on nucleation, growth, and overall deposition morphology.

Owing to the different passivating interphases (e.g., structure and composition), the Mg deposition morphology varies in different single-salt based electrolytes (e.g., "whisker-shaped" in $Mg(OTf)_2$ electrolyte and "seaweed-shaped" in $Mg(TFSI)_2$ electrolyte). Interestingly, after modifying these blank electrolytes with additives, a stark morphological transition to well-defined hexagonal Mg plates is observed in all modulated electrolytes with suppressed surface passivation (Fig. 5f). Indeed, hexagonal plate-shaped Mg deposition are preferential formed across various electrolyte chemistries, suggesting that this morphology is the intrinsically favorable deposition form of Mg metal in the absence of passivation. These findings could also explain why Mg anode was previously regarded as dendrite-free since the passivation is suppressed in most of the reported electrolyte systems applicable for MMBs under normal working conditions (e.g., moderate current densities and limited areal capacities). While a comprehensive investigation into the current density effects lies beyond the scope of this initial study, we additionally observed that the hexagonal plates morphology is consistently maintained across a wide range of plating rates (0.1, 0.25, 1, and 2 $mA\,cm^{-2}$) in the $Mg(OTf)_2 + MgCl_2$ electrolyte system (Supplementary Figs. 37–40). This result is consistent with previously reported fractal deposits composed of aggregated hexagonal platelets formed under high current densities in Grignard-based electrolytes[25,56], further verifying that the energetically favorable deposition morphology of HCP Mg metal prevails under different working conditions once surface passivation is suppressed.

Discussion

This study provides a conceptual framework for understanding and controlling Mg deposition behavior by establishing an explicit relationship between electrolyte composition, interphase chemistry, and the resulting deposit morphology. Our cryo-TEM observations reveal that effective suppression of surface passivation in different electrolyte systems enables a consistent morphological transition to plate-shaped structure, thereby exposing the intrinsic deposition tendencies of HCP Mg metal. This mechanistic insight, uniquely enabled by cryogenic nanoscale visualization and cross-electrolyte comparisons, challenges the long-standing view that deposition behavior in Mg systems is governed solely by electrolyte formulations and/or current densities. Instead, our findings underscore the pivotal role of interfacial chemistry in dictating Mg deposition behavior. Therefore, future study on the deposition process in multivalent metal systems should focus not only on modulating electrolyte properties but also on tailoring the interfacial ion transport kinetics with minimized passivation. Such efforts will be key to unlocking controlled, reversible metal growth and advancing the practical implementation of high-performance multivalent battery systems.

Our work resolves two long-standing controversial issues for Mg electrodeposition, i.e., it is widely believed that: (1) whisker-shaped dendrites are not prone to form on Mg anodes and (2) Mg deposition behavior is governed by different electrolyte chemistries. Using a representative conventional $Mg(OTf)_2$ electrolyte, we demonstrate an unexpected whisker-shaped Mg deposition process and unravel the detailed structure of the accompanying passivation layer on Mg deposits. By suppressing surface passivation through electrolyte modification, our cryo-TEM studies reveal the intrinsic deposition morphology of Mg metal to be a well-defined hexagonal platelet, which persists independent of electrolyte chemistries (i.e., salts, solvents or solvation structures) and in agreement with the theoretical Wulff structure prediction of HCP metals. The integration of cryo-TEM observations with multiscale simulations provides a fundamental understanding of the electrochemical behavior of Mg deposition correlating with the surface interphase in different electrolyte systems, which may offer avenues for designing high-performance electrolytes for durable MMBs.

Methods

Electrolyte preparation

DME (99.5%, anhydrous, Sigma-Aldrich) solvent was dried with molecular sieves (3 Å beads, 4–8 mesh, Sigma-Aldrich) for at least 24 h prior to electrolyte preparation. For the blank electrolytes using conventional Mg salts, 0.2 M of $Mg(OTf)_2$ (99.5%, Solvionic), $Mg(TFSI)_2$ (99.5%, Solvionic) and $Mg(HMDS)_2$ (97%, Sigma-Aldrich) were weighted directly into glass vials, respectively, followed by addition of DME solvent. The mixtures were stirred overnight until the solution became clear. The electrolytes modified with chloride-based $MgCl_2$ (anhydrous, ≥98%, Sigma-Aldrich) and chloride-free $TBABH_4$ (98%, Sigma-Aldrich) additives were prepared using the similar processes. The concentration of additives is fixed to be 0.1 M for $Mg(OTf)_2$ and $Mg(HMDS)_2$ based electrolytes. For $Mg(TFSI)_2$ based electrolytes, the additive amounts range from 0.1 M to 0.4 M. The additional APC and $Mg[B(hfip)_4]_2$ based electrolytes were prepared according to the reported methods[45,46]. For the preparation of APC electrolyte: 0.267 g $AlCl_3$ (anhydrous, 99.999%, Sigma-Aldrich) was dissolved in 3 mL tetrahydrofuran (THF, anhydrous, >99.9%, Sigma-Aldrich). After thoroughly dissolved, 2 mL phenylmagnesium chloride solution (2 M in THF, Sigma-Aldrich) was slowly dripped into the $AlCl_3$/THF solution and additionally stirred for 12 h. All the preparation steps were performed in an argon (Ar)-filled glovebox (O_2 < 1 ppm, H_2O < 0.1 ppm). For the preparation of $Mg[B(hfip)_4]_2$ salt: 2 mL di-n-butylmagnesium solution (1.0 M in heptane, Sigma-Aldrich) was first added to a 50 mL round-bottom flask. Subsequently, 0.43 mL 1,1,1,3,3,3-Hexafluoro-2-propanol (HFIP, ≥99 %, Sigma-Aldrich) was slowly added, followed by stirring for 5 h at 25 °C. Next, 4 mL DME was introduced into the solution, after which 4.1 mL borane tetrahydrofuran complex solution (1.0 M solution in THF, Sigma-Aldrich) was further added to the flask. Then, 1.42 mL HFIP was slowly added, and the mixture was stirred for 12 h. Finally, 20 mL hexane was added to precipitate the pure $Mg[B(hfip)_4]_2$ salt. After removing the hexane, the product was vacuum-dried at 40 °C for 12 h to yield a white crystalline powder. All the preparation steps were performed in an Ar-filled glovebox (O_2 < 1 ppm, H_2O < 0.1 ppm). All chemicals were used as received without further purification. All solvents were additionally dried over molecular sieves, and all Mg salts and additives were vacuum-dried prior to use in an Ar-filled glovebox (O_2 < 1 ppm, H_2O < 0.1 ppm) at 25 °C. We quantified the water contents in the prepared electrolytes using Karl Fischer titration (Metler-Toledo). As shown in Supplementary Table 1, the water amounts in all measured electrolytes were consistently below 15 ppm, and the addition of $MgCl_2$ would not increase the water amounts in the base electrolytes. A comparative overview of the electrolyte systems employed in this work was shown in Supplementary Table 2 and discussed in Supplementary Note 3.

Electrochemical measurements

The electrochemical performance was evaluated using 2032-type coin cells with 316 stainless steel spring (15.4 mm diameter, 1.1 mm height and 0.2 mm thickness, MTI) on Neware Battery Tester (CT-4008T-5V10mA) at 25 °C. The asymmetric cell was assembled with a Cu foil (1 cm^2) (≥ 99.8%, 12 µm thickness, MTI) as the working electrode, a Mg disk (1.26 cm^2) (99.9%, 100 µm thickness, MTI) polished by a blade as the counter electrode, and a layer of glass fiber (GF) separator (Whatman™ GF/A, 16 mm diameter, 260 µm thickness and 1.6 µm pore size) filled with 75 µL of electrolyte solution. In the symmetric cell configuration, the Cu foil was replaced with polished Mg disks (1.26 cm^2). The galvanostatic cycling measurements of symmetric cells with different electrolytes were conducted under working conditions of 0.5 mA cm^{-2} and 0.5 mAh cm^{-2}. All coin cell components were washed with isopropanol and acetone and dried overnight in 60 °C oven.

Characterization of the diffusion coefficient for electrolytes

The CC method was used to measure the diffusion coefficient of the Mg cations in the electrolyte. The potential at the working electrode was held at −0.5 V for 300 s to allow reduction of the Mg cations at electrode surface. Integration of current density over time was obtained and plotted against the square root of time as shown in Supplementary Fig. 27. To ensure accurate analysis, we performed the linear fitting only on the latter portion of the Anson plots, where the charge (Q) versus $t^{1/2}$ relationship becomes visibly and statistically linear. By excluding the initial non-linear segment and focusing on the linear region at longer times, we minimized the influence of non-diffusive effects. The slope extracted from this linear portion was then used to calculate the diffusion coefficient based on the Cottrell equation.

$$Q = \frac{2nFAC_0D^{\frac{1}{2}}}{\pi^{\frac{1}{2}}}t^{\frac{1}{2}} + Q_{dl} + Q_{ads} \quad (1)$$

where n is the number of charge transfer for reduction process happened at the surface (for the reduction process of Mg, $n = 2$), F is Faraday constant, A is the electrode area, C_O is the initial concentration of cation in electrolyte, Q_{dl} is the capacitive charge and Q_{ads} is the charge from the adsorbed species. Q is the integration of the current density during the working time, which is proportional to the square root of time.

Characterization of the diffusion coefficient for surface interphases

For assessment of the Mg-ion diffusion behavior in surface interphases, EIS was carried out on an asymmetric cell at open circuit potential (OCP) after depositing at 0.5 mA cm^{-2} for 15 min with a frequency range of 1 MHz to 0.1 Hz, 10 points per decade of frequency, and a perturbation amplitude of 5 mV by a Gamry electrochemical workstation (Reference 600 +). The impedance data was fit to an equivalent circuit commonly used to describe surface interphases, which consists of a capacitor representing the space charge capacitance (C_{SC}), a resistor representing the resistance to Mg^{2+} transport through the surface interphase (R_{Int}), and a capacitor representing the dielectric response of the surface interphase in parallel (C_{Int}). A Warburg diffusion element representing Mg^{2+} diffusion through the surface interphase is also included in series with the space charge capacitance. The interfacial charge transfer kinetics (that is, $Mg^{2+} + 2e^- \rightarrow Mg^0$) was neglected in this equivalent circuit based on previous studies suggesting that this is a reasonable approximation[22,57].

The Nernst-Einstein framework of ionic conductivity was used to calculate the ionic transport parameters of the interphase layer. The conductivity of the interphase layer is calculated via $\lambda_{Int} = \frac{l_{Int}}{R_{Int}A}$, where l_{Int} is the measured thickness of the interphase layer from cryo-TEM

and A is the electrode area. Traditionally, the Nernst-Einstein equation establishes a relationship between ionic conductivity and ion diffusion coefficients. Thus, experimental measurements of interphase conductivity can be used to calculate ion diffusion coefficients according to the Nernst-Einstein equation, which has been widely adopted by the battery community. With the λ_{Int} and the Warburg element (Z_W) from the equivalent circuit fitting, the diffusion coefficient of Mg^{2+} through the interphase layer ($D^{Int}_{Mg^{2+}}$) is calculated by the following Eq. (2).

$$D^{Int}_{Mg^{2+}} = \left(\lambda_{Int} Z_W A\right)^2 \quad (2)$$

The Mg-ion diffusion behavior in $Mg(OTf)_2 + MgCl_2$ electrolyte was further examined by LSV measurement. During the LSV measurement, the electrode was swept from OCP to about −0.7 V vs Mg/Mg^{2+} at scan rates of 0.1 V s^{-1} to 0.5 V s^{-1}. The $D_{Mg^{2+}}$ was calculated using the following equation:

$$i_p = 299000\alpha^{0.5} C_{Mg^{2+}} D^{\frac{1}{2}}_{Mg^{2+}} \upsilon^{\frac{1}{2}} \quad (3)$$

where i_p is the diffusion-limited peak of current density, υ is the scan rate, $C_{Mg^{2+}}$ is the bulk concentration of the Mg^{2+}, and α is the transfer coefficient, which is estimated as 0.5 in the absence of actual measurements[58,59].

Cryo-TEM characterization

For the sample preparation, 2032-type coin cells were assembled with a TEM Cu grid incorporated onto the Cu foil as the working electrode and Mg metal (99.9%, 100 µm thickness, MTI) as the counter/reference electrode. Each cell had 75 µL of electrolyte added with a GF/A separator. Mg metal was deposited onto the working electrode by applying a fixed current density of 0.5 mA cm^{-2} for different deposition time. After deposition, the TEM grid was disassembled from the coin cell in an Ar-filled glove box (H_2O < 0.1 ppm and O_2 < 1 ppm) at 25 °C. The grid was slightly rinsed with DME solvent to remove trace electrolyte. After vacuum-drying, the sample was transferred into cryo-TEM holder (Gatan Inc.) within the Ar-filled glove box (H_2O < 0.1 ppm and O_2 < 1 ppm), and closed the shuttle on the holder. The cryo-TEM holder was protected by an Ar protection sealed container, and quickly inserted into TEM column (the air-exposure time is less than 1 s). After sample insertion, the cryo-transfer holder maintains the grid temperature at approximately −178 °C. Cryo-TEM images were acquired in Thermo Fisher 300 kV Titan TEM equipped with a Gatan OneView CMOS camera (Gatan Inc.) with EDS capability. During the cryo-TEM imaging, electron flux is less than 100 e $Å^{-2}$ s^{-1} for low-magnification TEM images and less than 1000 e $Å^{-2}$ s^{-1} for high-resolution TEM images. The electron beam exposure time of each image is no more than 60 s, and the acquisition time is 0.4 s to 1 s. The electron doses on all presented images are summarized in Supplementary Table 4. The calculation method is shown in Supplementary Note 2

Materials characterization

The normal morphology was studied using SEM (JEOL 7600 F). Scanning transmission electron microscopy (STEM) high-angle annual dark-field (HAADF) images were acquired using Tecnai 200 kV with an Annular Dark Field detector (Fischione Instruments Inc.). For compositional analysis, elemental mapping of all samples was performed using an EDS detector (Ametek Inc.). EELS images were acquired using Tecnai with a Gatan imaging filter (GIF) detector (Gatan, Inc., Pleasanton, CA, USA). The camera length for the EELS measurement was kept at 43 mm. The TEM images and EELS data were processed using a Digital Micrograph plugin within the Gatan Microscopy Suite (GMS). The cross-sectional TEM samples between the Mg deposits and current collector were prepared by focused-ion-beam assisted scanning electron microscopy (FIB-SEM, Helios NanoLab 450 S, 30 KeV and 2.5 nA for cutting).

Theoretical simulations

The AIMD simulations were performed within the framework of density functional theory (DFT) as implemented in the Vienna Ab initio Simulation Package (VASP)[60,61]. The Perdew-Burke-Ernzerhof (PBE) exchange-correlation functional was employed[62], and long-range van der Waals interactions were accounted for via the DFT-D3 dispersion correction[63]. Projector augmented-wave (PAW) potentials were used to describe the core-valence interactions[64], and a plane-wave basis set with a cutoff energy of 400 eV was adopted. The structure was relaxed until atomic forces were less than 0.04 eV $Å^{-1}$, and the total energy difference was less than 10^{-4} eV. The Mg(0001) surface was modeled as a 5-layer slab in a 4 × 4 supercell with a 15 Å vacuum region. The initial configuration of liquid electrolyte was generated with PACKMOL package[65]. AIMD simulation were then run for 6 ps at 300 K using a 1 fs time step under an NVT ensemble, with temperature control via the Nosé-Hoover thermostat[66,67]. Only the Γ-point was sampled in reciprocal space.

The MD simulations were carried out using the Forcite software package. The Universal Forcefield (UFF)[68] was employed to describe the phase energy surface (PES), while atomic charge were assigned using the Charge Equilibration (Q_{eq}) method[69] with a tolerance of 5×10^{-4} e. The non-bond interaction was evaluated by the Ewald method[70] with an Ewald accuracy of 10^{-5} kcal/mol. During the geometry optimization, all the atoms were allowed to relax. The convergence criteria were set to 2×10^{-5} kcal mol^{-1} for energy change and 0.001 kcal mol^{-1} $Å^{-1}$ for force. Following geometry optimization, a 1 ns of NVT simulation was performed, followed by a 2 ns of NPT simulations, both with a time step of 1 fs. The data was collected in the production phase for 100 ns. Temperature control was implemented via the Andersen method[71], and pressure regulation was maintained using Berendsen method[72] during the simulation.

The phase field modelling is performed by COMSOL Multiphysics software based on the finite element method. The Mg deposition simulations were conducted in a 6 µm × 6 µm square region, where the bottom boundary presents the current collector, and the top boundary presents the bulk electrolyte with Mg ion concentration of $c_O = 0.2$ mol L^{-1}. A phase field model involving Butler-Volmer electrodeposition kinetics was developed to simulate the Mg deposition on Mg metal anodes. A phase field order parameter ξ was introduced to describe Mg deposition process: ξ = 1 for Mg metal phase, ξ = 0 for electrolyte phase, 0 < ξ < 1 for a numerical diffuse interface at phase interface between Mg metal and electrolyte. More details about the phase-field equations for this work can be found in the Supplementary Note 1.

Data availability

All data supporting the findings of this study are available within the article and its Supplementary Information files. Source data are provided with this paper.

References

1. Liang, Y., Dong, H., Aurbach, D. & Yao, Y. Current status and future directions of multivalent metal-ion batteries. *Nat. Energy* **5**, 646–656 (2020).
2. Zhang, H., Qiao, L. & Armand, M. Organic Electrolyte Design for Rechargeable Batteries: From Lithium to Magnesium. *Angew. Chem. Int. Ed.* **61**, e202214054 (2022).
3. Eng, A. Y. S. et al. Theory-guided experimental design in battery materials research. *Sci. Adv.* **8**, eabm2422 (2022).
4. Muldoon, J., Bucur, C. B. & Gregory, T. Quest for nonaqueous multivalent secondary batteries: magnesium and beyond. *Chem. Rev.* **114**, 11683–11720 (2014).
5. Sun, Y., Ai, F. & Lu, Y. C. Electrolyte and Interphase Design for Magnesium Anode: Major Challenges and Perspectives. *Small* **18**, e2200009 (2022).

6. Attias, R., Salama, M., Hirsch, B., Goffer, Y. & Aurbach, D. Anode-Electrolyte Interfaces in Secondary Magnesium Batteries. *Joule* **3**, 27–52 (2019).
7. Li, Y. et al. The contrast between monovalent and multivalent metal battery anodes. *Science* **389**, eadl5482 (2025).
8. Dong, K. et al. Unravelling the Mechanism of Lithium Nucleation and Growth and the Interaction with the Solid Electrolyte Interface. *ACS Energy Lett.* **6**, 1719–1728 (2021).
9. Cheng, X.-B. et al. A Review of Solid Electrolyte Interphases on Lithium Metal Anode. *Adv. Sci.* **3**, 1500213 (2016).
10. Attias, R. et al. Determination of Average Coulombic Efficiency for Rechargeable Magnesium Metal Anodes in Prospective Electrolyte Solutions. *ACS Appl. Mater. Interfaces* **14**, 30952–30961 (2022).
11. Wang, H. et al. Reversible Electrochemical Interface of Mg Metal and Conventional Electrolyte Enabled by Intermediate Adsorption. *ACS Energy Lett.* **5**, 200–206 (2020).
12. Zhang, J. et al. The origin of anode–electrolyte interfacial passivation in rechargeable Mg-metal batteries. *Energy Environ. Sci.* **16**, 1111–1124 (2023).
13. Dou, H. et al. Revisiting the degradation of solid/electrolyte interfaces of magnesium metal anodes: Decisive role of interfacial composition. *Nano Energy* **86**, 106087 (2021).
14. Li, Y. et al. Toward waterproof magnesium metal anodes by uncovering water-induced passivation and drawing water-tolerant interphases. *Nat. Commun.* **15**, 9364 (2024).
15. Kwak, J. H. et al. Operando Visualization of Morphological Evolution in Mg Metal Anode: Insight into Dendrite Suppression for Stable Mg Metal Batteries. *ACS Energy Lett.* **7**, 162–170 (2022).
16. Hu, X.-C. et al. Insight into interfacial processes and degradation mechanism in magnesium metal batteries. *Nano Energy* **78**, 105338 (2020).
17. Schick, B. W. et al. Influence of Chloride and Electrolyte Stability on Passivation Layer Evolution at the Negative Electrode of Mg Batteries Revealed by operando EQCM-D. *Angew. Chem. Int. Ed.* **63**, e202413058 (2024).
18. Hou, S. et al. Solvation sheath reorganization enables divalent metal batteries with fast interfacial charge transfer kinetics. *Science* **374**, 172–178 (2021).
19. Rajput, N. N., Qu, X., Sa, N., Burrell, A. K. & Persson, K. A. The Coupling between Stability and Ion Pair Formation in Magnesium Electrolytes from First-Principles Quantum Mechanics and Classical Molecular Dynamics. *J. Am. Chem. Soc.* **137**, 3411–3420 (2015).
20. Zachman, M. J., Tu, Z., Choudhury, S., Archer, L. A. & Kourkoutis, L. F. Cryo-STEM mapping of solid-liquid interfaces and dendrites in lithium-metal batteries. *Nature* **560**, 345–349 (2018).
21. Li, Y. et al. Atomic structure of sensitive battery materials and interfaces revealed by cryo–electron microscopy. *Science* **358**, 506–510 (2017).
22. Yuan, X., Liu, B., Mecklenburg, M. & Li, Y. Ultrafast deposition of faceted lithium polyhedra by outpacing SEI formation. *Nature* **620**, 86–91 (2023).
23. Jäckle, M., Helmbrecht, K., Smits, M., Stottmeister, D. & Groß, A. Self-diffusion barriers: possible descriptors for dendrite growth in batteries?. *Energy Environ. Sci.* **11**, 3400–3407 (2018).
24. Hagopian, A., Doublet, M.-L. & Filhol, J.-S. Thermodynamic origin of dendrite growth in metal anode batteries. *Energy Environ. Sci.* **13**, 5186–5197 (2020).
25. Davidson, R. et al. Formation of Magnesium Dendrites during Electrodeposition. *ACS Energy Lett.* **4**, 375–376 (2018).
26. Eaves-Rathert, J., Moyer, K., Zohair, M. & Pint, C. L. Kinetic- versus Diffusion-Driven Three-Dimensional Growth in Magnesium Metal Battery Anodes. *Joule* **4**, 1324–1336 (2020).
27. Li, S. et al. Cation replacement method enables high-performance electrolytes for multivalent metal batteries. *Nat. Energy* **9**, 285–297 (2024).
28. Zhang, D. et al. Constructing Efficient $Mg(CF_3SO_3)_2$ Electrolyte via Tailoring Solvation and Interface Chemistry for High-Performance Rechargeable Magnesium Batteries. *Adv. Energy Mater.* **13**, 2301795 (2023).
29. Chen, J. et al. The Metamorphosis of $Mg(SO_3CF_3)_2$-based Electrolytes for Rechargeable Magnesium Batteries. *ChemElectroChem* **11**, e202300664 (2024).
30. Yang, G. et al. In Situ Formed Magnesiophilic Sites Guiding Uniform Deposition for Stable Magnesium Metal Anodes. *Nano Lett.* **22**, 9138–9146 (2022).
31. Zhang, D. et al. Deeping insight of $Mg(CF_3SO_3)_2$ and comprehensive modified electrolyte with ionic liquid enabling high-performance magnesium batteries. *Nano Energy* **109**, 108257 (2023).
32. Ling, C., Banerjee, D. & Matsui, M. Study of the electrochemical deposition of Mg in the atomic level: Why it prefers the non-dendritic morphology. *Electrochim. Acta* **76**, 270–274 (2012).
33. Yang, G. et al. Realizing horizontal magnesium platelet deposition and suppressed surface passivation for high-performance magnesium metal batteries. *Energy Environ. Sci.* **17**, 1141–1152 (2024).
34. Han, B. et al. Probing the Na metal solid electrolyte interphase via cryo-transmission electron microscopy. *Nat. Commun.* **12**, 3066 (2021).
35. Connell, J. G. et al. Tuning the Reversibility of Mg Anodes via Controlled Surface Passivation by H_2O/Cl^- in Organic Electrolytes. *Chem. Mater.* **28**, 8268–8277 (2016).
36. Mohtadi, R., Tutusaus, O., Arthur, T. S., Zhao-Karger, Z. & Fichtner, M. The metamorphosis of rechargeable magnesium batteries. *Joule* **5**, 581–617 (2021).
37. Nguyen, D.-T. et al. A High-Performance Magnesium Triflate-based Electrolyte for Rechargeable Magnesium Batteries. *Cell Rep. Phy. Sci.* **1**, 100265 (2020).
38. Shterenberg, I. et al. Evaluation of $(CF_3SO_2)_2N$–(TFSI) Based Electrolyte Solutions for Mg Batteries. *J. Electrochem. Soc.* **162**, A7118 (2015).
39. Liao, C. et al. The unexpected discovery of the $Mg(HMDS)_2/MgCl_2$ complex as a magnesium electrolyte for rechargeable magnesium batteries. *J. Mater. Chem. A* **3**, 6082–6087 (2015).
40. Zheng, J. et al. Reversible epitaxial electrodeposition of metals in battery anodes. *Science* **366**, 645–648 (2019).
41. Wang, G. et al. Achieving Planar Electroplating/Stripping Behavior of Magnesium Metal Anode for a Practical Magnesium Battery. *ACS Energy Lett.* **9**, 48–55 (2023).
42. Zheng, J. et al. Regulating electrodeposition morphology of lithium: towards commercially relevant secondary Li metal batteries. *Chem. Soc. Rev.* **49**, 2701–2750 (2020).
43. See, K. A. et al. The Interplay of Al and Mg Speciation in Advanced Mg Battery Electrolyte Solutions. *J. Am. Chem. Soc.* **138**, 328–337 (2016).
44. Horia, R., Nguyen, D.-T., Eng, A. Y. S. & Seh, Z. W. Using a Chloride-Free Magnesium Battery Electrolyte to Form a Robust Anode–Electrolyte Nanointerface. *Nano Lett.* **21**, 8220–8228 (2021).
45. Mizrahi, O. et al. Electrolyte Solutions with a Wide Electrochemical Window for Rechargeable Magnesium Batteries. *J. Electrochem. Soc.* **155**, A103 (2008).
46. Mandai, T. Critical Issues of Fluorinated Alkoxyborate-Based Electrolytes in Magnesium Battery Applications. *ACS Appl. Mater. Interfaces* **12**, 39135–39144 (2020).
47. Guo, R. & Gallant, B. M. Li_2O Solid Electrolyte Interphase: Probing Transport Properties at the Chemical Potential of Lithium. *Chem. Mater.* **32**, 5525–5533 (2020).

48. Gu, Y. et al. Unraveling the Mechanism of Very Initial Dendritic Growth Under Lithium Ion Transport Control in Lithium Metal Anodes. *Nano Lett.* **23**, 9872–9879 (2023).
49. Boyle, D. T. et al. Resolving Current-Dependent Regimes of Electroplating Mechanisms for Fast Charging Lithium Metal Anodes. *Nano Lett.* **22**, 8224–8232 (2022).
50. Agarwal, G. et al. Insights into Spontaneous Solid Electrolyte Interphase Formation at Magnesium Metal Anode Surface from Ab Initio Molecular Dynamics Simulations. *ACS Appl. Mater. Interfaces* **13**, 38816–38825 (2021).
51. Chen, X.-R. et al. A Diffusion-Reaction Competition Mechanism to Tailor Lithium Deposition for Lithium-Metal Batteries. *Angew. Chem. Int. Ed.* **59**, 7743–7747 (2020).
52. Li, G. et al. Stable metal battery anodes enabled by polyethylenimine sponge hosts by way of electrokinetic effects. *Nat. Energy* **3**, 1076–1083 (2018).
53. Zhao, Y. et al. Effect of Mg Cation Diffusion Coefficient on Mg Dendrite Formation. *ACS Appl. Mater. Interfaces* **14**, 6499–6506 (2022).
54. He, Y. et al. Origin of lithium whisker formation and growth under stress. *Nat. Nanotechnol.* **14**, 1042–1047 (2019).
55. Liu, Z. et al. Dendrite-free Lithium Based on Lessons Learned from Lithium and Magnesium Electrodeposition Morphology Simulations. *Cell Rep. Phy. Sci.* **2**, 100294 (2021).
56. Davidson, R. et al. Mapping mechanisms and growth regimes of magnesium electrodeposition at high current densities. *Mater. Horiz.* **7**, 843–854 (2020).
57. Boyle, D. T. et al. Transient Voltammetry with Ultramicroelectrodes Reveals the Electron Transfer Kinetics of Lithium Metal Anodes. *ACS Energy Lett.* **5**, 701–709 (2020).
58. Attari, V., Banerjee, S. & Arroyave, R. On the kinetics of electrodeposition in a magnesium metal anode. *Acta Mater.* **276**, 120089 (2024).
59. Tian, H.-K. et al. Tuning the performance of a Mg negative electrode through grain boundaries and alloying toward the realization of Mg batteries. *J. Mater. Chem. A* **9**, 15207–15216 (2021).
60. Geerlings, P., De Proft, F. & Langenaeker, W. Conceptual density functional theory. *Chem. Rev.* **103**, 1793–1874 (2003).
61. Nagy, Á Density functional theory and application to atoms and molecules. *Phys. Rep.* **298**, 1–79 (1998).
62. Perdew, J. P., Burke, K. & Ernzerhof, M. Generalized gradient approximation made simple. *Phys. Rev. Lett.* **77**, 3865–3868 (1996).
63. Grimme, S., Antony, J., Ehrlich, S. & Krieg, H. A consistent and accurate ab initio parametrization of density functional dispersion correction (DFT-D) for the 94 elements H-Pu. *J. Chem. Phys.* **132**, 154104 (2010).
64. Blöchl, P. E. Projector augmented-wave method. *Phys. Rev. B* **50**, 17953–17979 (1994).
65. Martínez, L., Andrade, R., Birgin, E. G. & Martínez, J. M. PACKMOL: A package for building initial configurations for molecular dynamics simulations. *J. Comput. Chem.* **30**, 2157–2164 (2009).
66. Nosé, S. A unified formulation of the constant temperature molecular dynamics methods. *J. Chem. Phys.* **81**, 511–519 (1984).
67. Hoover, W. G. Canonical dynamics: Equilibrium phase-space distributions. *Phys. Rev. A* **31**, 1695 (1985).
68. Rappe, A. K. et al. a full periodic table force field for molecular mechanics and molecular dynamics simulations. *J. Am. Chem. Soc.* **114**, 10024–10035 (1992).
69. Rappe, A. K. & Goddard, W. A. I. I. I. Charge equilibration for molecular dynamics simulations. *J. Chem. Phys.* **95**, 3358–3363 (1991).
70. Karasawa, N. & Goddard, W. A. I. I. I. Acceleration of convergence for lattice sums. *J. Chem. Phys.* **93**, 7320–7327 (1989).
71. Andersen, H. C. Molecular dynamics simulations at constant pressure and/or temperature. *J. Chem. Phys.* **72**, 2384–2393 (1980).
72. Berendsen, H. J. C., Postma, J. P. M., van Gunsteren, W. F., DiNola, A. & Haak, J. R. Molecular dynamics with coupling to an external bath. *J. Chem. Phys.* **81**, 3684–3690 (1984).

Acknowledgements

Z.W.S. acknowledges the Singapore National Research Foundation (NRF Investigatorship NRF-NRFI09-0002) and the Agency for Science, Technology and Research (MTC Programmatic Fund M23L9b0052). G.Yu acknowledges the support from the Welch Foundation Award F-1861, Norman Hackerman Award in Chemical Research.

Author contributions

G. Yang and Z.W.S. conceived the project. G. Yang prepared the manuscript and performed the experiments. G.Yang and T.G. conducted the cryo-TEM characterization. Yuanjian Li, Z.C., and J. W. helped with data analysis. Z.J., C.Y.J.L., W.R. and Z.W.S. revised the manuscript. J. D. and Ying Li conducted AIMD simulation. C.Z. and W.L. performed the COMSOL simulations. Y.Y., G.Yu and Z.W.S. supervised the project. All authors discussed the results and commented on the manuscript.

Competing interests

The authors declare no competing interests.

Additional information

Supplementary information The online version contains supplementary material available at https://doi.org/10.1038/s41467-025-67029-4.

Correspondence and requests for materials should be addressed to Yan Yao, Guihua Yu or Zhi Wei Seh.

Peer review information *Nature Communications* thanks Tylan S. Watkins, and the other, anonymous, reviewer(s) for their contribution to the peer review of this work. A peer review file is available.